Small Structures

small structures

www.small-structures.com

RESEARCH ARTICLE OPEN ACCESS

Chemo-Mechanical Behavior of High- and Mid-Ni Cathodes in Sulfide-Based All-Solid-State Batteries: Who Will Prevail?

Choyeon Kim[1] | Min June Son[1] | Hyerim Kim[2] | Hyoju Lee[3] | Shizhao Xiong[4] | Dominic Bresser[5,6] | Yun-Chae Jung[7] | Jang-Yeon Hwang[2,3] | Un-Hyuck Kim[1]

[1]Department of Energy Science and Engineering, Daegu Gyeongbuk Institute of Science and Technology (DGIST), Daegu, Republic of Korea | [2]Department of Energy Engineering, Hanyang University, Seoul, Republic of Korea | [3]Department of Battery Engineering, Hanyang University, Seoul, Republic of Korea | [4]Faculty of Material Science and Engineering, Kunming University of Science and Technology, Kunming, China | [5]Helmholtz Institute Ulm (HIU), Ulm, Germany | [6]Karlsruhe Institute of Technology (KIT), Karlsruhe, Germany | [7]Advanced Batteries Research Center, Korea Electronics Technology Institute, Seongnam, Gyeonggi, Republic of Korea

Correspondence: Dominic Bresser (dominic.bresser@kit.edu) | Yun-Chae Jung (yunchae.jung@keti.re.kr) | Jang-Yeon Hwang (jangyeonhw@hanyang.ac.kr) | Un-Hyuck Kim (unhyuck.kim@dgist.ac.kr)

Received: 25 February 2026 | **Revised:** 24 May 2026 | **Accepted:** 6 July 2026

Keywords: all-solid-state batteries | chemo-mechanical interface stabilities | layered oxide cathodes | surface coatings | voltage restrictions

ABSTRACT

Achieving high energy densities in sulfide-based all-solid-state batteries (ASSBs) is fundamentally constrained by the coupled chemo-mechanical degradation of layered oxide cathodes, driven by lattice instability and interfacial chemical reactivity with solid electrolytes. Herein, by reinterpreting conventional lithium-ion battery design principles, we systematically evaluate two contrasting strategies: voltage-restricted operation of a high-nickel cathode (NCM811 at 4.2 V) and high-voltage operation of a mid-nickel cathode (NCM622 at 4.4 V). Using pressure-resolved electrochemical measurements, *operando* mechanical analysis, and interfacial spectroscopic characterization, we show that limiting the NCM811 upper cut-off voltage effectively suppresses the H2–H3 phase transition, minimizing lattice volume fluctuations and preserving the intrinsic mechanical and chemical stability even without surface protection. In contrast, NCM622 high-voltage operation induces deep delithiation accompanied by pronounced lattice contraction and accelerated sulfide electrolyte oxidative decomposition, leading to severe interfacial degradation and capacity fading. Applying a boron-based (B-based) surface coating to NCM622 significantly suppresses parasitic interfacial reactions, enabling substantial performance recovery and energy densities comparable to those of voltage-restricted high-nickel systems. These results decouple the roles of mechanical instability and chemical interfacial degradation, establishing a flexible cathode design framework that combines voltage window optimization for high-nickel cathodes with targeted interfacial engineering for high-voltage mid-nickel cathodes in ASSBs.

1 | Introduction

The ongoing electrification of modern technologies is no longer confined to electric vehicles but is rapidly extending to critical infrastructures such as energy storage systems for artificial intelligence data centers and power sources for humanoid and service robotics [1, 2]. Unlike automotive applications, these emerging platforms require noninterruptible operation over extended timescales that often span decades, imposing stringent requirements on rechargeable batteries. In particular, absolute safety

Choyeon Kim and Min June Son contributed equally to this study.

against thermal runaway must be ensured without compromising energy density or long-term durability [3–5]. All-solid-state batteries (ASSBs) employing nonflammable inorganic solid electrolytes have attracted considerable attention as a promising approach to overcome the intrinsic safety limitations of conventional lithium-ion batteries (LIBs) [6, 7]. Among the various solid electrolyte families, sulfide-based electrolytes, such as argyrodite Li_6PS_5Cl (LPSCl), are widely regarded as the most practical option because of their high lithium-ion conductivity, favorable mechanical compliance, and compatibility with cold-pressing-based fabrication processes [8, 9].

Despite substantial progress in the development of sulfide solid electrolytes (SSE), rational optimization of cathode active materials for ASSBs remains underexplored [10–12]. The selection of cathode compositions has largely followed the design principles established for liquid-electrolyte LIBs, where high-Ni layered oxides ($LiMO_2$ with Ni content exceeding 80%, M═Ni, Co, and Mn) are favored to meet aggressive energy density targets [5, 13, 14]. However, the solid-state environment imposes fundamentally different constraints. In liquid-electrolyte systems, interfacial contact loss arising from anisotropic lattice volume changes can be partially alleviated through electrolyte wetting and redistribution. Solid–solid interfaces lack such self-healing mechanisms. As a result, even modest anisotropic volume changes during cycling can lead to irreversible contact loss at the cathode–electrolyte interface, exacerbating mechanical degradation pathways that are largely buffered in liquid systems. To address these challenges, extensive efforts have focused on interfacial and morphological engineering strategies, including protective oxide coatings and single-crystal particle designs [15–17]. Such approaches have proven effective in improving interfacial stability, but they primarily operate as mitigation strategies rather than addressing the intrinsic origins of chemo-mechanical instability [18–23]. Consequently, the compositional and electrochemical operating parameters of layered oxide cathodes, which fundamentally govern both energy storage and mechanical response, warrant renewed scrutiny in the context of ASSBs.

A key unresolved question concerns the optimal nickel content for layered oxide cathodes under solid-state operating conditions. In conventional LIBs, mid-Ni cathodes, such as $Li[Ni_{0.6}Co_{0.2}Mn_{0.2}]O_2$ (NCM622), can achieve competitive energy densities when operated at elevated upper cut-off voltages, while offering advantages in thermal stability and cycle life compared with their high-Ni counterparts [5, 24]. Whether this high-voltage mid-Ni strategy is viable in sulfide-based ASSBs and whether high-Ni compositions are essential despite their mechanical vulnerabilities have not been systematically examined.

This study was designed to address whether a single cathode composition can realistically satisfy the diverse and often conflicting performance requirements of sulfide-based ASSBs. Rather than assuming a universally optimal material, we investigated the selection of cathode composition and operating voltage based on specific application-driven requirements. Specifically, this study examines the compositional conditions necessary for stable operation at commercially relevant energy densities, with an emphasis on cost efficiency and mechanical robustness, and the conditions requiring alternative cathode design strategies to achieve high energy density and fast charge–discharge operation. By systematically comparing high-Ni such as $Li[Ni_{0.8}Co_{0.1}Mn_{0.1}]O_2$ (NCM811) and mid-Ni layered oxides across different voltage windows under controlled pressure conditions, this study aims to establish composition- and operation-specific design guidelines for cathode materials for next-generation solid-state battery systems.

2 | Results and Discussion

2.1 | Morphological and Structural Evolution of Mid- and High-Ni NCM Cathodes

The synthesized cathode materials were categorized into two distinct groups based on their Ni fractions: mid-Ni cathodes ($Li[Ni_{0.5}Co_{0.2}Mn_{0.3}]O_2$ (NCM523) and NCM622) and high-Ni cathodes (NCM811 and $Li[Ni_{0.9}Co_{0.05}Mn_{0.05}]O_2$ (NCM90)) [13, 24]. The chemical compositions were quantitatively verified using inductively coupled plasma optical emission spectroscopy (ICP-OES), and the results were in good agreement with the designed stoichiometries (Table S1). Scanning electron microscopy (SEM) was used to characterize morphological features. The top-view SEM images revealed that all secondary particles possessed a highly spherical geometry (Figures 1a–d and S1). To minimize variations in the cathode–solid electrolyte interfacial contact area, the average particle diameter (D_{50}) of all samples was controlled at 10–11 μm (Figure S2). This ensured that the observed differences originated primarily from the intrinsic properties of the cathode materials rather than differences in particle size.

The precursor calcination temperatures were systematically modulated to optimize the crystallinity for each composition: 950 °C for NCM523, 850 °C for NCM622, 800 °C for NCM811, and 760 °C for NCM90 [5]. Cross-sectional SEM analysis indicated that this thermal history directly governed the primary particle size (Figure 1a1–d1). While the mid-Ni cathodes synthesized at higher temperatures consisted of coarser primary particles, their high-Ni counterparts exhibited densely packed microstructures composed of refined primary particles smaller than 400 nm (Figures 1e and S3). Powder X-ray diffraction (XRD) analysis confirmed that all synthesized cathode materials crystallized in a well-defined layered structure. The diffraction patterns could be consistently indexed to an O3-type structure that is crystallographically analogous to the hexagonal α-$NaFeO_2$ framework and belongs to the $R\bar{3}m$ space group, indicating phase-pure layered ordering across the entire compositional range. To further quantify the subtle structural variations induced by Ni content, Rietveld refinement was performed on the XRD patterns (Figure 1f–i and Table S2). With an increase in the Ni fraction, a systematic increase in the average Ni oxidation state is expected, leading to a reduced population of Ni^{2+} species. As Ni^{2+} exhibits an ionic radius comparable to that of Li^+, its suppression effectively mitigates Li/Ni cation mixing within the layered lattice [25]. This compositional evolution is reflected in the lattice parameters; the *a*-axis gradually expands because of the larger ionic radius of Ni^{3+} relative to Mn^{4+}, whereas the *c*-axis contracts because of the diminished cation disorder and enhanced interlayer ordering (Figures 1j and S4) [26]. The quantitative refinement results corroborate this trend, revealing a

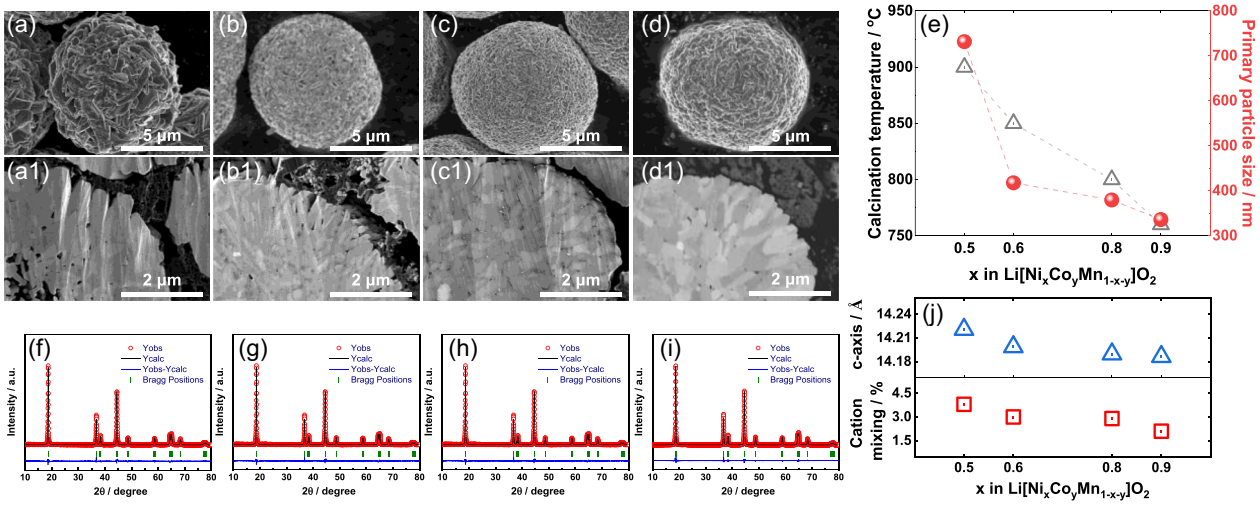

FIGURE 1 | Powder scanning electron microscopy (SEM) images of (a) NCM523, (b) NCM622, (c) NCM811, and (d) NCM90; cross-sectional SEM images of (a1) NCM523, (b1) NCM622, (c1) NCM811, and (d1) NCM90; (e) correlation between calcination temperature and size of primary particle; observed and calculated powder X-ray Rietveld refinement profiles for (f) NCM523, (g) NCM622, (h) NCM811, and (i) NCM90; (j) crystallographic properties as a function of Ni contents: *c*-axis, cation mixing.

monotonic decrease in Li/Ni cation mixing from ≈4% in NCM523 to ≈2% in NCM90. Collectively, these results demonstrate that the high-Ni cathodes synthesized in this study maintain a highly ordered layered structure with minimal cation disorder despite the relatively low synthesis temperatures, providing a structurally robust platform for subsequent electrochemical evaluation.

2.2 | Electrochemical Response of Mid- and High-Ni Cathodes in ASSBs

To establish a reliable electrochemical baseline before their integration into all-solid-state systems, the fundamental electrochemical performances of the synthesized cathodes were first evaluated using liquid electrolyte-based coin half-cells, followed by corresponding assessments in all-solid-state configurations employing SSE (LPSCl). All the cathodes were tested without surface coating in both systems to probe their intrinsic electrochemical behavior without the influence of interfacial modification layers.

The reversible capacity of layered oxide cathodes increases linearly with increasing Ni content [5]. Consistent with previous reports, the discharge capacities of all four cathode compositions, NCM523, NCM622, NCM811, and NCM90, exhibited a clear linear dependence on the Ni fraction when evaluated across multiple upper cut-off voltages at a fixed lower cut-off voltage, as well as across different C rates (0.1 and 0.5 C). Detailed procedures for the cell assembly and specific electrochemical testing conditions for each battery configuration are provided in the Experimental section. Linear regression analysis yielded coefficients of determination (R^2) exceeding 0.92 in every case (Figure S5) [14, 27]. These results demonstrate that the synthesized cathodes exhibit well-controlled and composition-consistent electrochemical behavior, providing a robust baseline for subsequent evaluations in ASSB configurations.

To evaluate the intrinsic electrochemical properties of the cathodes and the cathode LPSCl interface, pressure-controllable test cells were used, maintaining a constant stacking pressure of 35 MPa. This approach ensured intimate physical contact between the active materials and the solid electrolyte, thereby minimizing contact resistance artifacts [28, 29]. At a low current density of 0.1 C, the initial discharge capacities measured at a cut-off voltage of 4.2 V exhibited a strong linear correlation with the Ni content ($R^2 = 0.97$), delivering 134.5, 149.9, 180.0, and 183.8 mAh g^{-1}, respectively (Figure 2a). This linearity was well maintained when the cut-off voltage was increased to 4.3 V ($R^2 = 0.97$) (Figure 2b). However, further increasing the voltage to 4.4 V produced a slight deviation from linearity ($R^2 = 0.94$), primarily because of the lower expected capacity of NCM90 (Figure 2c). This capacity shortfall was likely caused by the formation of interfacial voids and particle disintegration, which resulted from severe surface parasitic reactions and anisotropic lattice volume expansion under high-voltage operation (Figure S6). In this process, a significant Ni fraction was oxidized to the highly reactive Ni^{4+} state [14, 30, 31]. Notably, increasing the current density to 0.5 C produced a significant collapse of the linear relationship between capacity and composition. Although the correlation remained moderate at 4.2 V ($R^2 = 0.83$), it deteriorated sharply at higher voltages, decreasing to $R^2 = 0.37$ at 4.3 V and becoming negligible at 4.4 V ($R^2 = 0.15$) (Figures 2a–c and S7). This drastic deviation indicates that high-Ni cathodes, particularly NCM90, experience severe kinetic limitations and contact loss under combined high-voltage and high-rate conditions, which prevent them from delivering their intrinsic capacities (Figure S8) [32, 33]. Cycle-life analysis further elucidated the voltage-dependent nature of the degradation. When cycled at 4.2 V, where the detrimental H2–H3 phase transition is largely suppressed [34], NCM811 demonstrated relatively stable performance with a capacity retention of 88.0% after 50 cycles, whereas NCM90 retained only 74.4% (Figure 2d). When the cut-off voltage was increased to 4.3 and 4.4 V, the mid-Ni cathode NCM622 exhibited superior structural resilience, retaining 86.9% and 84.3% of its initial capacity, respectively. In contrast, under the

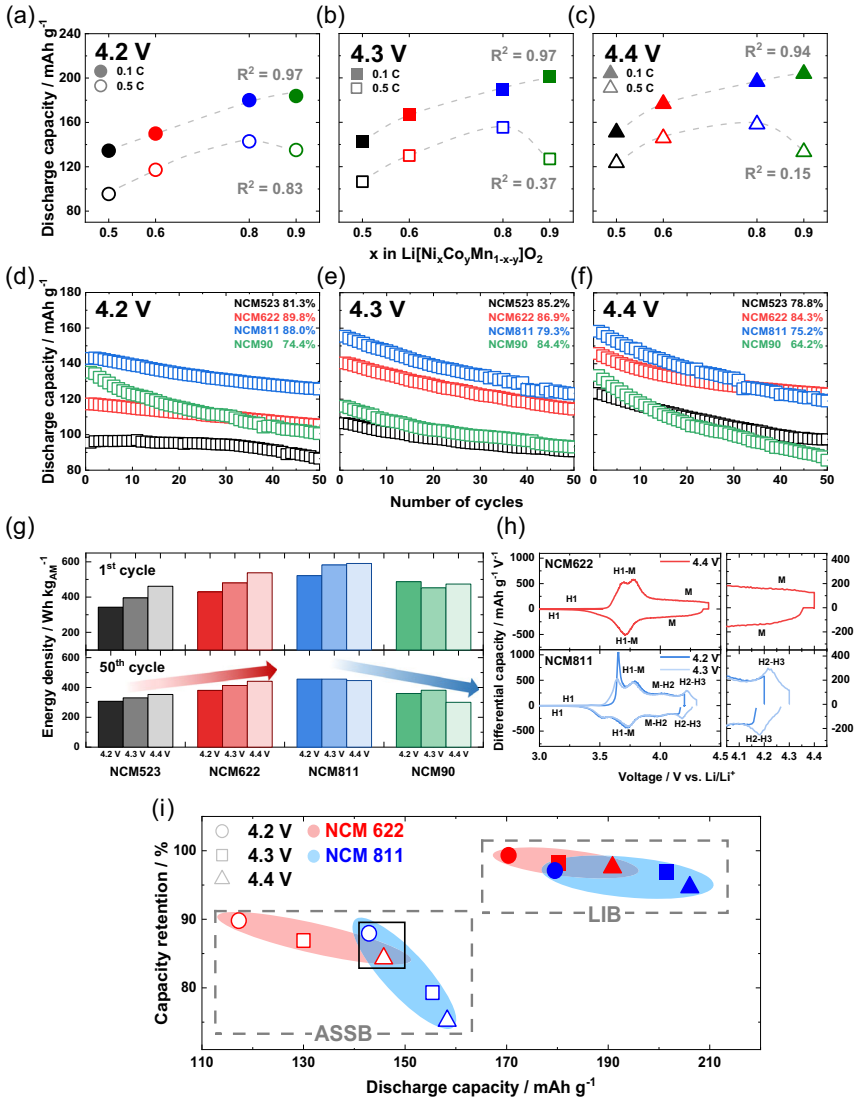

FIGURE 2 | Comparison of 0.1 C discharge capacity and 0.5 C discharge capacity of ASSBs at 30 °C under upper cut-off voltages of (a) 4.2, (b) 4.3, and (c) 4.4 V as a function of Ni contents (x in $Li[Ni_xCo_yMn_{1-x-y}]O_2$); 0.5 C discharge capacity under upper cut-off voltage of (d) 4.2 V, (e) 4.3 V, and (f) 4.4 V; (g) energy density of the cathode active material in ASSBs at the 1st and 50th cycles; (h) dQ dV^{-1} profiles of NCM622 (top panel) and NCM811 (bottom panel) at different upper cut-off voltages, highlighting the distinct H2–H3 phase transition in NCM811; and (i) comparison of discharge capacity and cycling stability between NCM622 and NCM811 in LIBs and ASSBs.

same 4.3 and 4.4 V cut-off conditions, NCM811 showed accelerated degradation, and the capacity retention decreased to 79.3% and 75.2% (Figure 2e,f).

To further clarify the voltage-dependent phase evolution underlying these electrochemical trends, differential capacity (dQ dV^{-1}) analysis was performed (Figure S9). When the upper cut-off voltage was limited to 4.2 V, the NCM90 cathode ceased charging within a regime where the H2–H3 phases began to coexist. This led to an electrochemically unstable voltage plateau and increased susceptibility to kinetic polarization. NCM811 operated at 4.2 V was confined to a state preceding the H2–H3 phase transition, thereby avoiding severe lattice contractions and maintaining a comparatively stable electrochemical response (Figure S9a, b). When the cut-off voltage was increased to 4.3 and 4.4 V, both NCM811 and NCM90 exhibited clear signatures of the H2–H3 phase transition in their dQ dV^{-1} profiles, consistent with the accelerated capacity fading observed at higher voltages (Figure S9c–f). In contrast, mid-Ni cathodes such as NCM523 and NCM622 displayed smooth, continuous dQ dV^{-1} features across the entire voltage range from 4.2 to 4.4 V, without evidence of distinct phase transitions, in agreement with their solid solution-type behavior reported in conventional layered oxide systems [35]. These results indicate that the electrochemical instability of high-Ni cathodes at elevated voltages originates from abrupt phase transitions, whereas mid-Ni cathodes retain phase continuity but become increasingly vulnerable to chemo-mechanical degradation under deep delithiation conditions.

Based on these results, the gravimetric energy densities (Wh kg_{AM}^{-1}) were calculated while accounting for the voltage decay during cycling. The analysis reveals a distinct trade-off: mid-Ni cathodes, such as NCM523 and NCM622, achieve tangible gains in energy density through voltage elevation, both initially

and after 50 cycles. High-Ni cathodes, including NCM811 and NCM90, do not scale with increasing voltage because of accelerated chemo-mechanical degradation (Figures 2g and S10) [14]. This observation leads to a key research question regarding ASSB cathode design: whether better overall performance can be achieved by driving mid-Ni cathodes to higher voltage windows of 4.4 V or by limiting high-Ni cathodes to more stable voltage limits of 4.2 V. To further clarify the voltage-dependent phase evolution underlying these electrochemical trends, a detailed differential capacity ($dQ\ dV^{-1}$) analysis was performed (Figure 2h). As clearly visualized in the profiles, the mid-Ni cathode (NCM622) maintains a broad, relatively featureless, and continuous redox behavior without abrupt phase transitions across the entire investigated voltage range up to 4.4 V. In stark contrast, the high-Ni cathode (NCM811) exhibits pronounced voltage sensitivity. When operated to 4.2 V, NCM811 remains within a stable solid-solution regime, characterized by the complete absence of the detrimental H2–H3 phase transition. However, upon increasing the cut-off voltage to 4.3 and 4.4 V, the emergence and evolution of the sharp H2–H3 transition peak becomes highly evident [14, 36].

Accordingly, the upper cut-off voltage of NCM811 was strategically limited to 4.2 V to evade the severe structural strain associated with the H2–H3 transition. Conversely, NCM622 was operated up to 4.4 V to achieve a comparable specific capacity under deep delithiation conditions. To rigorously evaluate the intrinsic stability limits of these contrasting design frameworks, NCM622 operated at 4.4 V and NCM811 operated at 4.2 V were selected for direct comparative analysis (Figures 2i and S11), as these two configurations deliver matched specific capacities while highlighting fundamentally different structural and operational states. In particular, the NCM622 cathode operated at 4.4 V and the NCM811 cathode operated at 4.2 V delivered closely matched discharge capacities at 0.1 C under ASSB conditions, as shown in Figure 2i, enabling a balanced, meaningful comparison between the two cathodes. Moreover, NCM622 and NCM811 are widely regarded as representative mid- and high-Ni layered cathodes, respectively. A direct comparison between high-voltage mid-Ni operation and voltage-restricted high-Ni operation allows the intrinsic electrochemical, mechanical, and interfacial characteristics of these two contrasting design strategies to be systematically evaluated, providing generalizable insights into the cathode selection principles for sulfide-based ASSBs.

2.3 | Chemo-Mechanical Behavior of Cathodes With Similar Capacity at Different Voltages

The stack pressure during galvanostatic cycling closely follows lithium insertion in the cathode active material, as shown in Figures 3a and S12a. During repeated lithiation and delithiation, the resulting volumetric expansion and contraction are largely reversible, causing periodic oscillations in mechanical stress throughout cycling.

As the applied current density increased, the specific capacity gradually decreased. Correspondingly, the net amplitude of the stress variation also decreased, indicating diminished lithium transport within the cathode. Although using a Li–In alloy anode generally results in significantly larger absolute stress levels than those of a zero-strain $Li_4Ti_5O_{12}$ counter electrode, the present configuration allows the contribution from the cathode volume change to be isolated: The partial molar volume of Li remained constant across the comparative conditions, and the total volume change due to the Li flux was normalized. As a result, the stress fluctuations superimposed on the baseline expansion of the anode can be attributed to the intrinsic chemo-mechanical breathing behavior of the cathode material (Figure S12b) [18, 37].

Figure 3a illustrates the *operando* evolution of the stack pressure for cells employing NCM622 (4.4 V) and NCM811 (4.2 V) cathodes during charging at C rates of 0.1, 0.2, and 0.5 C. In this cell configuration, the overall pressure response was dominated by the volumetric expansion of the Li–In alloy anode during plating. However, by controlling the lithium flux and normalizing the total capacity throughput across all measurements, the volumetric contribution of the anode can be regarded as constant. Therefore, any differences observed in the pressure profiles reflect differences in the intrinsic chemo-mechanical responses of the cathode materials.

Across the entire range of C rates investigated, the NCM811-based cell exhibited a higher net pressure build-up than the corresponding NCM622-based cell. Layered oxide cathodes undergo lattice contraction, which corresponds to a decreased volume upon delithiation; this contraction partially offsets the volumetric expansion of the anode. From this perspective, the larger net pressure increase observed for NCM811 indicates that the cathode underwent limited lattice contraction and provided minimal offset for the anode expansion. In contrast, the lower net pressure observed in the NCM622 cell indicates a significant decrease in total pressure, resulting from pronounced lattice contraction of the cathode. Relative to the constant anode baseline, these results indicate that NCM811 underwent markedly smaller cathode volume fluctuations than NCM622 and possesses superior mechanical stability during electrochemical cycling.

To directly validate this interpretation and identify the structural origin of the observed pressure change, in situ XRD measurements were performed using liquid electrolyte-based cells (Figure 3b,c).

Operating NCM622 at an elevated cut-off voltage of 4.4 V leads to deep delithiation and continuous unit cell volume shrinkage of ≈3.41% (Figure 3d). This pronounced lattice contraction was the primary source of its larger pressure variation during cycling. This behavior is consistent with previous reports indicating that pushing layered oxide cathodes to higher voltages causes greater volumetric shrinkage, even at comparable capacities, just as NCM622 exhibits larger contraction at high voltages compared to NCM811 operated at lower voltages [38]. In contrast, severe volume fluctuations in high-Ni cathodes originate primarily from the abrupt contraction of the *c*-axis during the high-voltage H2–H3 phase transition. Consistent with this mechanism, contour plots of the (003) diffraction peak show that NCM811 and NCM622 (Figure 3b,c), when operated with the upper cut-off voltage limited to 4.2 and 4.4 V, respectively, behave differently; NCM811 remains within a stable solid-solution regime preceding the onset of the H2–H3 phase transition, whereas NCM622 exhibits a severe peak shift attributed to excessive lattice delithiation [35]. As a result, the associated lattice volume

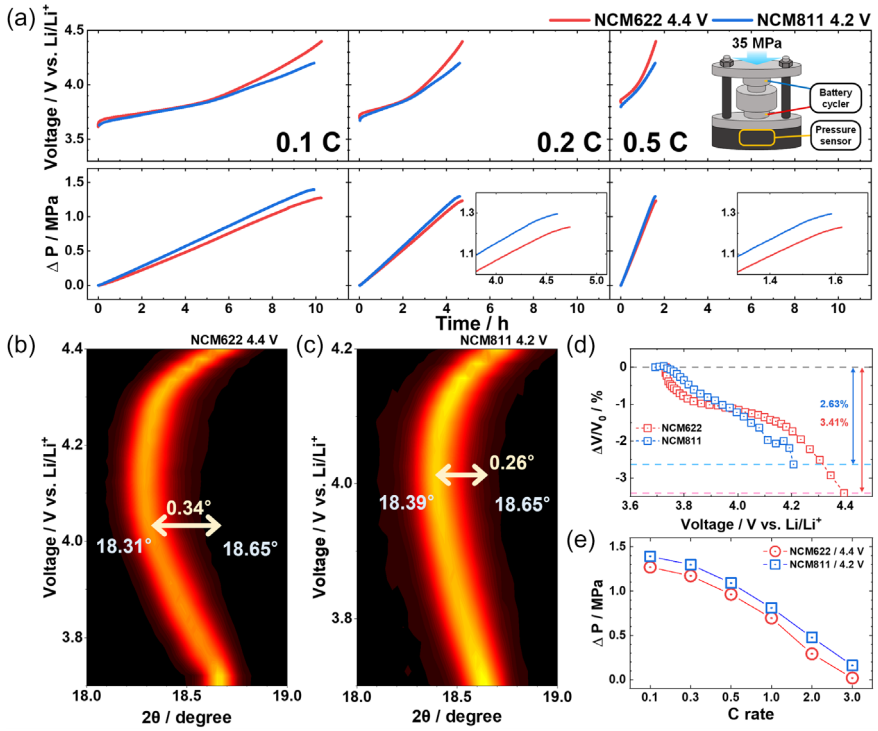

FIGURE 3 | (a) Voltage (upper panel) and pressure (lower panel) profiles of NCM622 and NCM811 as a function of time during the charge process; contour plot of in situ XRD analysis of (b) NCM622, (c) NCM811; (d) unit cell volume deviation, obtained using a liquid electrolyte-type pouch cell starting from 3.7 V at 0.05 C; and (e) value of pressure difference before and after the charge process regarding C rate.

change was effectively suppressed. This interpretation is supported by the corresponding dQ dV^{-1} inverse profiles provided in Figure S9, which lack the characteristic features associated with the H2–H3 transition under 4.2 V operation.

In addition to the structural effects, the operational voltage window critically dictates the surface stability. The operation of NCM622 at 4.4 V forces the material into a state of deep delithiation, which synergistically combines severe lattice contraction with increased surface reactivity toward the solid electrolyte and accelerates the parasitic interfacial reactions. In stark contrast, NCM811, restricted to 4.2 V, maintains a mechanically benign state; despite delivering a comparable specific capacity, it operates within a controlled state-of-charge window that minimizes both structural strain and interfacial reactivity (Figure S13). Consequently, as the C rate increased, the frequent parasitic reactions in the high-voltage regime intensified the structural distortion and interfacial resistance, introducing a kinetic barrier that hindered the reversibility of the NCM622 phase transition. The relative unit-cell volume variation shown in Figure S13c is intended to provide a comparative indication of cathode-induced chemo-mechanical evolution rather than a direct quantification of macroscopic electrode stress. The greater lattice contraction caused by this kinetic instability, combined with the enhanced chemical reactivity of the solid electrolyte, may increase the susceptibility of the electrode to mechanical degradation. This could potentially lead to microcracking and interfacial void formation. This chemo-mechanical instability is further supported by Figure 3e, which shows a large decrease in the pressure variation with increasing C rate [19]. In this context, operation within a high-Ni, low-voltage window is more effective for decoupling electrochemical performance from chemo-mechanical instability caused by deep delithiation.

2.4 | Postcycling Microstructure Degradation and Interfacial Contact Loss

To investigate the evolution of interfacial morphology and microstructure, cross-sectional SEM images of the NCM622 and NCM811 composite cathodes were acquired in the charged state at 4.4 and 4.2 V, respectively, after 50 charge–discharge cycles (Figures 4a,b and S14). In the NCM622 composite cycled to an upper cut-off voltage of 4.4 V, extensive void formation was observed at the cathode–solid electrolyte interface, resulting in pronounced contact loss. This degradation was further aggravated by the anisotropic volume changes inherent to NCM622 under high-voltage operation. In contrast, the NCM811 cathode cycled within a structurally controlled voltage window of ≈4.2 V exhibited mitigated microstructural damage with a void area fraction of only 3.8%. In comparison, the NCM622 cathode exhibited severe void propagation, with an area fraction of 7.6% (Figures 4c and S15). Consequently, a clear disparity in the interfacial coverage of the cathode–solid electrolyte was evident, amounting to 47.9% for structurally stable NCM811 and 14.6% for degraded NCM622 (Figures 4d and S16). The formation of interfacial voids and the associated reduction in contact coverage disrupted the grain boundary connectivity and induced partial physical detachment of the cathode from the solid electrolyte. This degradation increased the lithium-ion transport tortuosity, impeding ionic conduction and promoting spatially heterogeneous electrochemical activity [39–41]. Although the overall

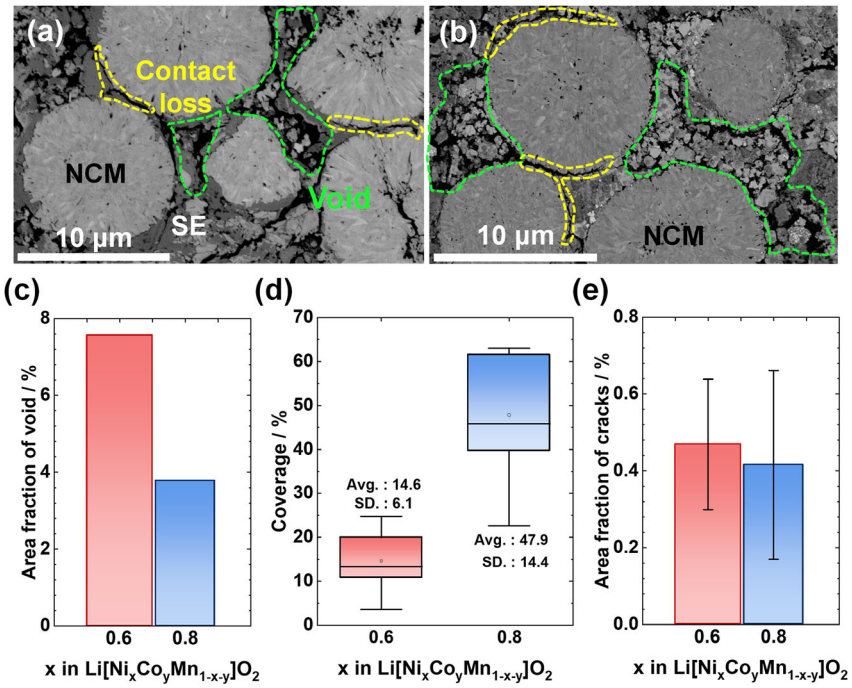

FIGURE 4 | Cross-sectional SEM images of the cathode composites after 50 cycles, charged to 4.4 and 4.2 V, respectively: (a) NCM622, (b) NCM811; quantification of NCM622 and NCM811 composite cathode: (c) area fraction of voids, (d) surface coverage, and (e) area fraction of cracks within secondary particles.

microcrack area fraction between the two cathodes remained comparable (Figures 4e and S17), the presence of interfacial voids facilitated nonuniform delithiation and exposed fresh surfaces that were more susceptible to parasitic chemical reactions with the solid electrolyte. Ultimately, progressive mechanical detachment rendered portions of the secondary particles electrochemically inactive, whereas cumulative propagation together with contact loss contributed to accelerated capacity decay and shortened cycle life.

2.5 | Chemical Degradation and Interfacial Stability Analysis

SSEs generally exhibit a limited electrochemical stability window, ≈1.7–2.3 V versus Li/Li^+, which is inherently mismatched with the operating voltage range of NCM cathodes [42]. This thermodynamic incompatibility promotes oxidative decomposition of the solid electrolyte at the cathode interface, leading to the formation of resistive interphases that impede lithium-ion transport [43–45]. In this study, the capacity-fading mechanisms caused by surface reactions at the cathode active material–electrolyte interface in ASSBs were systematically investigated, focusing on distinguishing the interfacial degradation behavior of mid-Ni cathodes operated at high voltages from that of high-Ni cathodes operated within restricted low-voltage windows.

Beyond mechanical degradation, electrochemical performance decay in ASSBs is strongly influenced by interfacial chemical instability. X-ray photoelectron spectroscopy (XPS) was performed to identify the chemical species generated during cycling. Figure 5 shows the S 2*p* and P 2*p* spectra of the pristine LPSCl electrolyte and cycled cathode composites. In the S 2*p* region, the doublet at 160.9 and 162.1 eV was assigned to Li_2S-related species, while the dominant doublet at 161.4 and 162.6 eV corresponds to the PS_4^{3-} tetrahedral units characteristic of the LPSCl structure. In addition, weaker doublets appearing at 162.9 and 164.1 eV, as well as at 163.9 and 165.1 eV, were attributed to P–S–P type linkages and elemental sulfur species, respectively (Figure 5a). In the P 2*p* region, the doublets observed at 132.0 and 132.8 eV are associated with the PS_4^{3-} tetrahedral units characteristic of the LPSCl structure. Minor doublets at 133.1 and 133.9 eV were assigned to P-containing polysulfide species (P_2S_x), whereas the signals at 134.2 and 135.0 eV correspond to oxygenated P species, such as Li_3PO_4 from the decomposition of the SSE (Figure 5b) [46, 47].

The emergence of P—S—P bonding motifs, such as those associated with P_2S_7 or P—S—S—P units, indicated the oxidative polymerization of thiophosphate anions, whereas the higher-binding-energy sulfur signal was consistent with the formation of thermodynamically stable elemental sulfur species. The degree of electrolyte decomposition was quantified by calculating the relative areal ratio of the oxidized sulfur species to the pristine PS_4^{3-} signal (Figure 5c,d). For the NCM622 cathode, this degradation ratio increased markedly, consistent with high-voltage operation, which promoted the accumulation of highly reactive Ni^{4+} species at the interface and accelerated oxidative electrolyte decomposition [48, 49]. The resulting decomposition products increase interfacial resistance and induce spatially heterogeneous electrochemical activity, which can further aggravate local contact degradation and void growth. Therefore, the severe void formation observed in high-voltage NCM622 is attributed to the coupled effects of mechanical contraction and chemical interfacial instability rather than to lattice contraction alone. In contrast, the NCM811 cathode exhibited a substantially lower

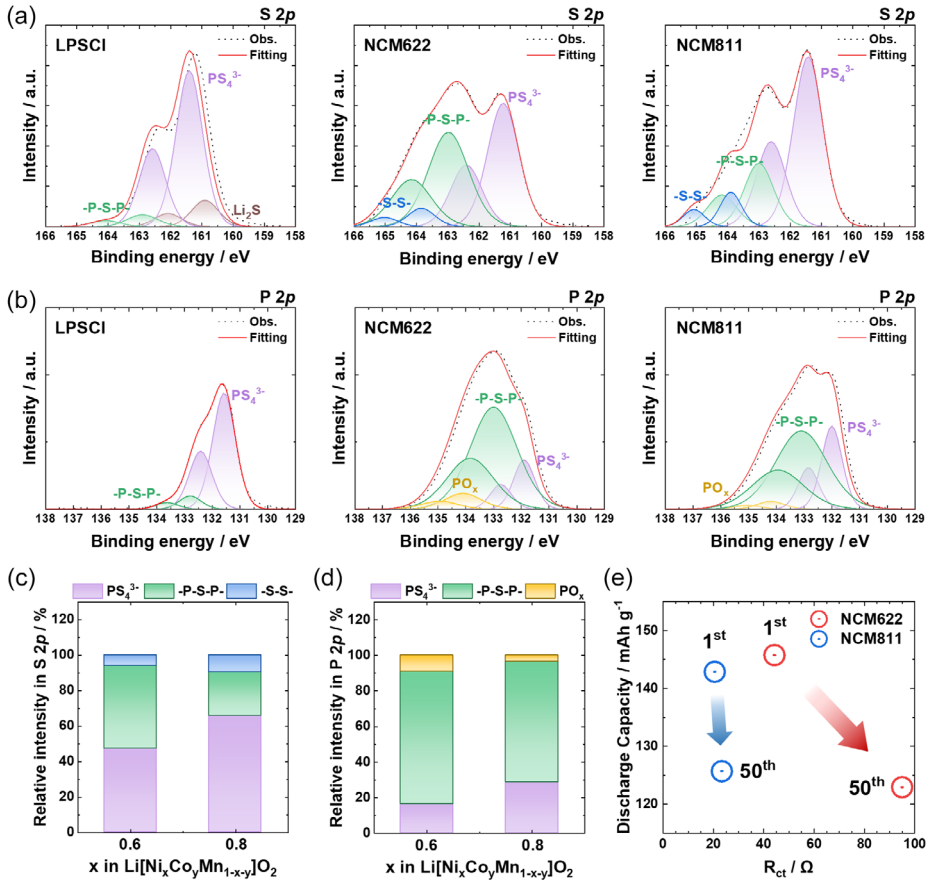

FIGURE 5 | X-ray photoelectron spectroscopy (XPS) spectra of LPSCl and NCM622, NCM811 after 50 cycles, charged to 4.4 and 4.2 V, respectively: (a) S 2*p*, (b) P 2*p*. The dashed and red solid lines represent the measured and fitted spectra, respectively. Quantitative evaluation of relative peak area ratios for (c) S 2*p* and (d) P 2*p* as a function of Ni content ($x = 0.6, 0.8$); (e) Discharge capacity and charge–transfer resistance of NCM622 and NCM811 after the 1st and 50th cycles, operated with upper cut-off voltages of 4.4 and 4.2 V, respectively.

degradation ratio, which remained above 50% even after cycling. Despite the higher nickel content, this suppressed interfacial reactivity was attributed to the restricted operating voltage window, which limited the formation of unstable surface species and preserved the cathode–electrolyte interfacial integrity.

These spectroscopic observations are consistent with the electrochemical impedance spectroscopy results shown in Figures 5e and S18. To quantitatively correlate the mechanical degradation with electrochemical impedance, the evolution of charge–transfer resistance was compared with the intrinsic lattice strain and interfacial void fraction. NCM622 exhibited a pronounced lattice contraction of 3.41%, accompanied by severe contact loss with a void fraction of 7.6% after 50 cycles, resulting in substantially increased impedance growth (50 Ω) and an elevated IR drop of 441.7 mV. In contrast, NCM811 maintained a smaller lattice contraction of 2.63%, a reduced void fraction of 3.8%, and a lower IR drop of 174.0 mV under the restricted voltage condition. These results indicate a clear correlation between lattice-driven contact degradation and electrochemical polarization in ASSBs. When considered together with the cross-sectional SEM evidence of interfacial void formation and coverage loss, these results indicate that chemical interfacial reactions and mechanical contact degradation were strongly coupled under the high-voltage operation of mid-Ni cathodes. In contrast, the NCM811 cathode operated within a restricted-voltage window of 4.2 V and maintained a comparatively stable interface, exhibiting suppressed interfacial degradation and a lower charge–transfer resistance without the need for additional surface modification [49, 50]. In this context, the present findings suggest that a high-Ni, low-voltage operating strategy provides a more intrinsically stable pathway for sulfide-based ASSBs, whereas mid-Ni cathodes operating at elevated voltages require the introduction of protective surface coatings or buffer layers to mitigate interfacial degradation and achieve comparable stability.

2.6 | Voltage-Dependent Interfacial Stabilization in NCM622 and NCM811 Cathodes

To further examine the interplay between the mechanical stability and interfacial chemical reactivity, the electrochemical performances of both cathode systems were evaluated after applying a boron-based (B-based) surface coating designed to selectively suppress reactions with the LPSCl solid electrolyte. XPS analysis together with transmission electron microscope (TEM) characterization confirmed the formation of a uniform $LiBO_2$ surface layer generated by the reaction between H_3BO_3 and the residual lithium species (LiOH and Li_2CO_3) on the NCM surface (Figures S19 and S20) [51–53].

In their pristine, uncoated states, the NCM811 cathode operated within a restricted-voltage window of 4.2 V exhibited superior

electrochemical performance and mechanical integrity compared to the NCM622 cathode cycled to 4.4 V. Upon introduction of the protective coating, both systems showed improved electrochemical performance; however, the extent of the improvement differed markedly between the two cathodes.

The NCM622 cathode operated at 4.4 V displayed a substantial capacity increase of 8.6% relative to its uncoated counterpart, whereas the NCM811 cathode operated at 4.2 V exhibited only a marginal improvement of 3.6% (Figure 6a,b,d,e). This contrast indicated that the NCM811 system already possessed a high degree of intrinsic structural and chemical stability when operated within a thermodynamically stable voltage window, limiting the benefits of additional surface protection. In contrast, the NCM622 cathode experienced pronounced surface degradation under high-voltage operation and therefore benefited more significantly from the parasitic interfacial reaction suppression afforded by the coating.

To substantiate these electrochemical trends, XPS was employed to track the evolution of interfacial degradation products. In the uncoated NCM622 cathode after cycling, the S 2*p* spectra show the emergence of distinct doublet features associated with the P–S–P-type bonding motifs (162.9 eV) and polysulfide species (163.9 eV). The P 2*p* spectra exhibited distinct doublet features corresponding to P-S-P-type bonding motifs (133.1 eV) and phosphate (PO_x) species (134.2 eV), providing direct evidence of the extensive oxidative decomposition of the sulfide electrolyte [46, 47]. In addition, pronounced signals corresponding to oxidized sulfur and phosphorus species, such as sulfate-like and phosphate-like moieties, were observed, which were attributed to reactions between the solid electrolyte and the oxygen released from the highly delithiated cathode surface [54–57]. In contrast, the coated NCM622 cathode showed a marked suppression of these decomposition-related features, particularly those associated with P–S–P linkages and oxidized species, confirming the effectiveness of the surface coating in mitigating interfacial

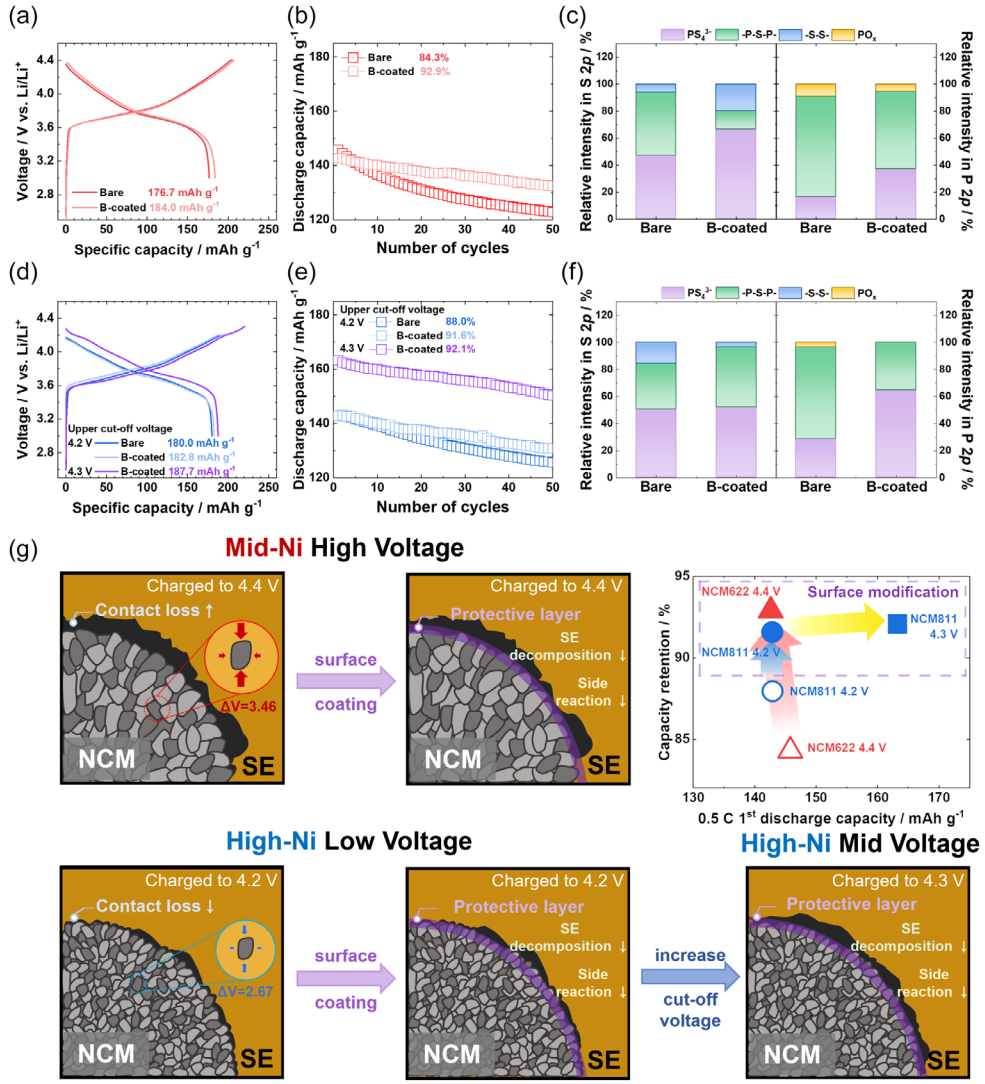

FIGURE 6 | Evaluation of the B-coating effect on $Li[Ni_xCo_yMn_{1-x-y}]O_2$ ($x = 0.6, 0.8$): electrochemical performance including initial charge–discharge profiles at 0.1 C for (a) NCM622 charged to 4.4 V and (d) NCM811 charged to 4.2, 4.3 V, and cycling performance for (b) NCM622 and (e) NCM811; XPS spectra of S 2*p* and P 2*p* for (c) NCM622 and (f) NCM811; (g) schematic illustration of the combined effect of voltage-restricted operation and chemical surface passivation proposed in this work.

chemical reactions (Figures 6c and S21a) [58, 59]. Notably, the NCM811 cathode exhibited intrinsically lower intensities of these degradation signals, even in the uncoated state, consistent with its reduced surface reactivity under restricted-voltage operation (Figures 6f and S21b). Importantly, although the surface coating does not eliminate the bulk H2–H3 phase transition at 4.3 V, it significantly improves its reversibility. By suppressing parasitic interfacial reactions, the coating promotes more homogeneous lithium extraction and insertion across the cathode surface, thereby reducing localized polarization and heterogeneous delithiation during cycling. This interfacial stabilization likely mitigates nonuniform structural strain, contributing to the improved reversibility of the H2–H3-related redox features observed in the dQ dV^{-1} profiles (Figure S22).

Building on these observations, we examined whether the operational voltage window of high-Ni cathodes could be extended by interfacial engineering alone. When the cut-off voltage of the B-coated NCM811 cathode was increased to 4.3 V, a voltage range typically associated with the onset of the H2–H3 phase transition, a pronounced enhancement in the electrochemical performance was observed. The coated NCM811 delivered a high specific capacity of 187.7 mAh g^{-1} at 0.1 C, despite the elevated cut-off voltage (Figure 6d). This improvement was preserved at higher current densities, with the cathode exhibiting a markedly increased capacity at 0.5 C and maintaining a capacity retention of 92.1% after 50 cycles (Figure 6e). This behavior indicates that although bare high-Ni cathodes are susceptible to instability at 4.3 V, effective surface passivation can substantially mitigate surface-initiated degradation processes. In particular, the B-based coating suppressed the excessive oxidation of Ni^{3+} to the highly reactive Ni^{4+} state at the cathode surface, reducing parasitic reactions with the sulfide electrolyte [52]. From a structural perspective, operation at 4.3 V allowed NCM811 to access a broader portion of the H2–H3 transition region; however, the lattice remained predominantly in the H2 phase with only partial involvement of the H3 phase [39]. In this regime, the associated mechanical strain was significant but remained tolerable because the interfacial chemical reactivity was effectively controlled. Importantly, these results demonstrate that the applicability of high-Ni cathodes in sulfide-based ASSBs is not strictly limited by conservative voltage restrictions. By employing targeted chemical surface passivation to suppress Ni oxidation and electrolyte decomposition without inducing particle cracking, the usable voltage window of high-Ni cathodes can be judiciously expanded to achieve higher capacities while preserving cycle stability. From a practical perspective, additional rate capability and low-temperature (0 °C) evaluations further supported the advantages of the voltage-restricted high-Ni strategy (Figures S23 and S24). NCM811 consistently exhibited higher capacity retention across all tested C rates together with improved recovery behavior compared to high-voltage-operated NCM622. At 0 °C, NCM811 also delivered a higher initial discharge capacity (148.3 vs. 138.0 mAh g^{-1}), although the cycling stability of both systems became relatively similar under kinetically limited conditions [60, 61]. In addition, NCM811 offers improved cost-effectiveness through reduced cobalt content compared to NCM622 [62]. These results further support the practical viability of the voltage-restricted high-Ni strategy for high-energy sulfide-based ASSBs. Overall, these results demonstrate a practical framework for the cathode design of sulfide-based ASSBs. Restricting the cut-off voltage of high-Ni cathodes has emerged as an effective standalone strategy for preserving both structural integrity and interfacial chemical stability. For mid-Ni cathodes, the challenges associated with high-voltage operation are evident, including lattice volume changes and accelerated interfacial degradation (Figure 6g). Nevertheless, the present findings demonstrate that simple surface passivation strategies can effectively suppress chemical side reactions, enabling mid-Ni cathodes to achieve energy densities comparable to those of high-Ni systems despite their intrinsic chemo-mechanical limitations.

3 | Conclusion

This study examined cathode operation strategies for ASSBs by directly comparing high-voltage mid-Ni and voltage-controlled high-Ni layered oxides. Although the high-voltage operation of mid-Ni cathodes is a dominant strategy in liquid-electrolyte LIBs, our results demonstrate that this approach is not intrinsically well suited to a rigid solid-state environment. NCM622 operated at 4.4 V suffered severe chemo-mechanical degradation driven by deep delithiation, anisotropic lattice contraction, and accelerated interfacial reactions. Although B-based surface passivation yielded a substantial capacity recovery of 8.6%, this heavy reliance on coatings underscores the structural vulnerability inherent to high-voltage mid-Ni operation in ASSBs. In contrast, the high-Ni cathode (NCM811) exhibited superior intrinsic stability under voltage-restricted operation. Limiting the cut-off voltage to 4.2 V confined NCM811 to the stable solid-solution regime, thereby preserving its mechanical integrity and interfacial stability even without surface modification (coating benefit limited to 3.6%). Furthermore, effective surface passivation unlocked the potential to extend the operating window to 4.3 V, thereby enabling higher reversible capacity while maintaining structural coherence. This confirms that high-Ni cathodes possess greater adaptability to the chemo-mechanical constraints of sulfide-based solid-state architectures. Overall, these findings suggest that cathode strategies optimized for liquid electrolytes cannot be directly applied to all-solid-state systems. Instead, high-Ni cathodes operating within carefully defined voltage windows, optionally supported by targeted interfacial engineering, represent the definitive and most scalable pathway toward achieving high energy density and long-term stability in sulfide-based ASSBs.

4 | Experimental Section

4.1 | Material Synthesis

Cathode active materials were prepared via calcination. For the targeted active material, $[Ni_xCo_yMn_{1-x-y}](OH)_2$ (Battery Solution) and $LiOH{\cdot}H_2O$ (Samchun Chemical, 99.99%) ((Ni + Co + Mn): Li = 1:1.01 molar ratio) were thoroughly mixed in an agate mortar for 30 min in a dry room. The mixture was then calcined under an oxygen atmosphere. Regardless of precursor, the initial calcination temperature was identical: 450 °C for 5 h. The next calcination temperature differed depending on the composition of the transition metal precursor: NCM523: 950 °C; NCM622: 850 °C; NCM811: 800 °C; NCM90: 760 °C for 10 h. The final

products were stored in an Ar-filled glove box ($O_2 < 0.1$ ppm, $H_2O < 0.1$ ppm). B-coated NCM622 and NCM811 were prepared by heating the active material and boron source. The as-synthesized active material and boric acid were mixed for 30 min at a molar ratio of 1:0.05 in an agate mortar. Then, the mixture was heated at 300 °C for 5 h under an oxygen atmosphere. The elemental compositions of transition metal precursors were verified with ICP-OES in an Agilent 5110 ICP-OES device. Particle size analysis was performed using an Anton Par PSA1090.

4.2 | Electrochemical Measurements

The cathode for the ASSBs was prepared by mixing the active material, LPSCl (POSCO JK Solid Solution), and Super C65 (Timcal) for 30 min at a ratio of 80:19:1 by weight. A Li–In alloy with a stoichiometry of $Li_{0.3}In$ was used as the anode for ASSBs by alloying In foil (100 μm, ø12, Nilaco) and Li metal (100 μm, ø6, Honjo). Nontreated Al and Ni foil were used as current collectors for the cathode and anode, respectively. First, LPSCl (150 mg) was compressed in a PEEK mold at 72 MPa. Then, 20 mg of composite cathode with an electrode density of 3.25 g cm^{-3} (active material loading: 12.05 mg cm^{-2}) was compressed together with the Al current collector under 370 MPa. The Li–In alloy and the Ni current collector were placed on opposite sides of the catholyte. Finally, external pressure measurements were performed using a custom-built force sensor. To measure the stack pressure, a calibrated force sensor was connected to a digital indicator. The initial stack pressure was applied using a precision torque wrench (TONE, Japan). For pressure analysis, the pressure variation (ΔP) in each cycle was calculated using the initial pressure at the beginning of charging as the baseline reference.

The cathode for the LIBs was prepared by mixing the active material, Super P, KS-6, and 6 wt% polyvinylidene fluoride in *N*-methyl pyrrolidone for 15 min at a ratio of 90:3.6:2.4:4 by weight. The resulting slurry was cast on Al foil with a Dr-blade and dried in a vacuum oven at 60 °C overnight. In the resulting cathode foil, the active material loading was 3–6 mg cm^{-2}. The slurry was then mixed and cast in a dry room. Li metal (200 μm, Honjo) and Celgard 2320 (Celgard) were used as anode and separator, respectively. 1.3 M $LiPF_6$ in ethylene carbonate-ethyl methyl carbonate-diethyl carbonate (3:5:2, vol%) with 0.5% (w/v) vinylene carbonate (PuriEL) was used as the electrolyte. Regardless of the cell type, the assembly process was performed in an Ar-filled glovebox ($O_2 < 0.1$ ppm, $H_2O < 0.1$ ppm).

All voltages reported in this study were referenced to the Li/Li^+ redox potential. All electrochemical measurements were cycled at 0.5 C (90 mA g^{-1}) after formation cycles at 30 °C. The formation cycles comprised two cycles at 0.1 C and one cycle at 0.2 C for ASSBs, and one cycle at 0.1 and 0.2 C for LIBs. The lower cut-off voltage varied depending on the cell: 3.0 V for ASSBs and 2.7 V for LIBs. The upper cut-off voltage varied according to the target voltage: 4.2, 4.3, and 4.4 V. The cycling test was performed on a CT3002 AU (Landt Instruments). Electrochemical impedance spectroscopy was performed after the galvanostatic and constant-voltage charge processes using an SP-200 Potentiostat (BioLogic).

4.3 | Analytical Approach

The powder XRD patterns were collected on a Rigaku MiniFlex 600 using Cu Kα radiation ($\lambda = 1.5406$ Å) source with 10°–80° 2θ range, a step of 0.02°, and 1.00 s of duration time. The collected patterns were analyzed using Rietveld refinement software (FullProf). To determine the change in the lattice constant during the charging process, in situ XRD measurements were conducted on pouch-type half-cells using lithium metal as the counter electrode. The cells were cycled between 3.7 and 4.4 V for NCM622 and 3.7–4.2 V for NCM811 at 0.05 C with galvanostatic charge. XRD patterns were collected every 20 min using a 1D detector (PIXcel 1D, PANalytical). To determine the side reactions between the active material and LPSCl, XPS was performed using an ESCALAB 250Xi instrument. The Al Kα radiation ($\lambda = 8.3386$ Å) source was used to scan the binding energy of the S 2*p* and P 2*p* orbitals with a spot size of 100×100 μm^2. XPS data were processed and analyzed using CasaXPS software. All the binding energies were calibrated to the adventitious carbon (C 1*s*) signal at 284.8 eV. Peak fitting was performed using a Shirley background and GL(30) line shapes. The cross-sectional milling of the active materials and ASSBs was performed using a cryogenic ion sample preparation system (JEOL, IB-19520CCP). Cross-sectional SEM images of the ASSBs were obtained in the charged state after 50 cycles. The microstructures of the precursor, active material, and cross-sectional electrode of the LIBs were examined using SEM (Helios, Thermo Fisher Scientific). Voids and cracks in the cross-sectional electrodes of the ASSBs were examined using SEM with a vacuum transfer holder. The widths and lengths of the primary particles of the cathode active materials were determined from cross-sectional SEM images of the active materials using image-processing software (ImageJ) [63]. The coverage between the active material and LPSCl, area fraction of voids, and cracks in the ASSBs were determined from the cross-sectional SEM images of the ASSBs. TEM (JEM ARM200F, JEOL) analysis was conducted to confirm the uniform B-coating layer. TEM sample prepared from as-synthesized B-coated powder was cut to 40 nm thickness using a focused ion beam (SCIOS, FEI) and loaded onto a Mo grid.

Author Contributions

Choyeon Kim: conceptualization (equal), methodology (equal), data curation (equal), investigation (equal), validation (equal), visualization (equal), formal analysis (equal). **Min June Son**: conceptualization (equal), methodology (equal), data curation (equal), investigation (equal), validation (equal), visualization (equal), formal analysis (equal). **Hyerim Kim**: formal analysis (equal), investigation (equal), resources (equal), visualization (equal). **Hyoju Lee**: formal analysis (equal), investigation (equal), resources (equal). **Shizhao Xiong**: Supervision (equal), writing – review & editing (equal). **Dominic Bresser**: supervision (equal), writing – review & editing (equal). **Yun-Chae Jung**: supervision (equal), writing – review & editing (equal). **Jang-Yeon Hwang**: supervision (equal), writing – review & editing (equal). **Un-Hyuck Kim**: supervision (equal), writing – review & editing (equal).

Acknowledgments

This research was supported by National Research Council of Science & Technology(NST) grant by the Korea government (MSIT) (No. GTL24011-000) and Korea Institute for Advancement of Technology (KIAT) grant

funded by the Korea Government (MOTIE) (RS-2026-25540388 and RS-2024-00417730 (HRD Program for Industrial Innovation)).

Funding

This work was supported by National Research Council of Science & Technology(NST) grant by the Korea government (MSIT) (No. GTL24011-000) and Korea Institute for Advancement of Technology (KIAT) grant funded by the Korea Government (MOTIE) (RS-2026-25540388 and RS-2024-00417730 (HRD Program for Industrial Innovation)).

Conflicts of Interest

The authors declare no conflicts of interest.

Data Availability Statement

The data that support the findings of this study are available from the corresponding author upon reasonable request.

References

1. M. C. Offutt, L. Zhu, and A. J. Lawson, "Data Centers and Their Energy Consumption: Frequently Asked Questions," *Congressional Research Service* 26 (2025): R48646, https://www.congress.gov/crs-product/R48646.

2. S. N. E. Research, "Technology Development Status and Market Outlook for Humanoid Robots and Robot Batteries (∼2040)," *SNE Research* (2026): 1969490, https://www.sneresearch.com/kr/business/report_view/252/page/0#ac_id.

3. D. P. Finegan, M. Scheel, J. B. Robinson, et al., "*In-operando* High-Speed Tomography of Lithium-Ion Batteries during Thermal Runaway," *Nature Communications* 6 (2015): 6924, https://doi.org/10.1038/ncomms7924.

4. L. Zhao, J. Hou, X. Feng, et al., "The Trade-Off Characteristic between Battery Thermal Runaway and Combustion," *Energy Storage Materials* 69 (2024): 103380, https://doi.org/10.1016/j.ensm.2024.103380.

5. H.-J. Noh, S. Youn, C. S. Yoon, and Y.-K. Sun, "Comparison of the Structural and Electrochemical Properties of Layered $Li[Ni_xCo_yMn_z]O_2$ (x = 0.8 and 0.85) Cathode Material for Lithium-Ion Batteries," *Journal of Power Sources* 233, no. 3 (2013): 121–130, https://doi.org/10.1016/j.jpowsour.2013.01.063.

6. F. Strauss, J. H. Teo, A. Schiele, et al., "Gas Evolution in Lithium-Ion Batteries: Solid versus Liquid Electrolyte," *ACS Applied Materials & Interfaces* 12 (2020): 20462–20468, https://doi.org/10.1021/acsami.0c02872.

7. X. Mu, H. Ding, Y. Wu, H. Hu, and B. Yu, "Nonflammable Liquid Electrolytes for Safe Lithium Batteries," *Small Structures* 4 (2023): 2300179, https://doi.org/10.1002/sstr.202300179.

8. H.-J. Deiseroth, S.-T. Kong, H. Eckert, et al., "Li_6PS_5X: A Class of Crystalline Li-Rich Solids With an Unusually High Li^+ Mobility," *Angewandte Chemie International Edition* 47 (2008): 755–758, https://doi.org/10.1002/anie.200703900.

9. A. Manthiram, X. Yu, and S. Wang, "Lithium Battery Chemistries Enabled by Solid-State Electrolytes," *Nature Reviews Materials* 2 (2017): 16103, https://doi.org/10.1038/natrevmats.2016.103.

10. T. Shi, Q. Tu, Y. Tian, et al., "High Active Material Loading in All-Solid-State Battery Electrode via Particle Size Optimization," *Advanced Energy Materials* 10 (2020): 1902881, https://doi.org/10.1002/aenm.201902881.

11. E. Schlautmann, J. Drews, L. Ketter, et al., "Graded Cathode Design for Enhanced Performance of Sulfide-Based Solid-State Batteries," *ACS Energy Letters* 10 (2025): 1664–1670, https://doi.org/10.1021/acsenergylett.4c03243.

12. X.-D. Zhang, F.-S. Yue, J.-Y. Liang, J.-L. Shi, H. Li, and Y.-G. Guo, "Structure Design of Cathode Electrodes for Solid-State Batteries: Challenges and Progress," *Small Structures* 1 (2020): 2000042, https://doi.org/10.1002/sstr.202000042.

13. H. Li, A. Liu, N. Zhang, et al., "An Unavoidable Challenge for Ni-Rich Positive Electrode Materials for Lithium-Ion Batteries," *Chemistry of Materials* 31 (2019): 7574–7583, https://doi.org/10.1021/acs.chemmater.9b02372.

14. H.-H. Ryu, K.-J. Park, C. S. Yoon, and Y.-K. Sun, "Capacity Fading of Ni-Rich $Li[Ni_xCo_yMn_{1-x-y}]O_2$ ($0.6 \leq x \leq 0.95$) Cathodes for High-Energy-Density Lithium-Ion Batteries: Bulk or Surface Degradation?," *Chemistry of Materials* 30 (2018): 1155–1163, https://doi.org/10.1021/acs.chemmater.7b05269.

15. F. Strauss, J. H. Teo, J. Maibach, et al., "Li_2ZrO_3-Coated NCM622 for Application in Inorganic Solid-State Batteries: Role of Surface Carbonates in the Cycling Performance," *ACS Applied Materials & Interfaces* 12 (2020): 57146–57154, https://doi.org/10.1021/acsami.0c18590.

16. S. Lee, D. Lee, and A. Manthiram, "Mixed Ionic-Electronic Conductivity of High-Nickel, Single-Crystal Cathodes Influencing the Cycling Stability of All-Solid-State Lithium-Ion Batteries," *Journal of Materials Chemistry A* 12 (2024): 26244–26252, https://doi.org/10.1039/d4ta03727h.

17. N.-Y. Park, H.-U. Lee, T.-Y. Yu, et al., "High-Energy, Long-Life Ni-Rich Cathode Materials with Columnar Structures for All-Solid-State Batteries," *Nature Energy* 10 (2025): 479–489, https://doi.org/10.1038/s41560-025-01726-8.

18. R. Koerver, W. Zhang, L. de, et al., "Chemo-Mechanical Expansion of Lithium Electrode Materials – on the Route to Mechanically Optimized All-Solid-State Batteries," *Energy & Environmental Science* 11 (2018): 2142, https://doi.org/10.1039/c8ee00907d.

19. D. Lee, Y. Shim, E. Choi, et al., "Alleviating Kinetical Delamination Induced by Localized Cathode Contact via Electrochemo-Mechanical Modeling in All-Solid-State Batteries," *Joule* 9 (2025): 102046, https://doi.org/10.1016/j.joule.2025.102046.

20. Z. Jiang, S. Li, M. Deng, et al., "Unravelling the Stabilization Effect of Fluorination on the Interface and Bulk Phase of Electrodes in All-Solid-State Lithium Metal Batteries," *Materials Today* 90 (2025): 31–42, https://doi.org/10.1016/j.mattod.2025.08.019.

21. C. Wei, Z. Wu, S. Li, et al., "Ultra-Efficient and Stable Janus Interface to Construct High-Performance Sulfide-Based All-Solid-State Lithium Metal Batteries," *Materials Science and Engineering: R: Reports* 164 (2025): 100950, https://doi.org/10.1016/j.mser.2025.100950.

22. Z. Wu, S. Wu, Z. Huang, et al., "Sulfide Redox Couple Enabled Dynamic Lattice-Oxygen Stabilization in Lithium-Rich Manganese Oxide All-Solid-State Batteries," *Cell Reports Physical Science* 7 (2026): 103112, https://doi.org/10.1016/j.xcrp.2026.103112.

23. Z. Wu, L. Du, T. Yang, et al., "Lithium Difluorophosphate Additive Engineering Enabling Stable Cathodic Interface for High-Performance Sulfide-Based All-Solid-State Lithium Battery," *Energy & Environmental Materials* 8 (2025): e12871, https://doi.org/10.1002/eem2.12871.

24. J.-H. Kim, K.-J. Park, S. J. Kim, C. S. Yoon, and Y.-K. Sun, "A Method of Increasing the Energy Density of Layered Ni-Rich $Li[Ni_{1-2x}Co_xMn_x]O_2$ Cathodes (x = 0.05, 0.1, 0.2)," *Journal of Materials Chemistry A* 7 (2019): 2694, https://doi.org/10.1039/c8ta10438g.

25. R. Kanno, H. Kubo, T. Kamiyama, et al., "Phase Relationship and Lithium Deintercalation in Lithium Nickel Oxides," *Journal of Solid State Chemistry* 110 (1994): 216, https://doi.org/10.1006/jssc.1994.1162.

26. K.-S. Lee, S.-T. Myung, K. Amine, H. Yashiro, and Y.-K. Sun, "Structural and Electrochemical Properties of Layered $Li[Ni_{1-2x}Co_xMn_x]O_2$ (x = 0.1–0.3) Positive Electrode Materials for Li-Ion

Batteries," *Journal of the Electrochemical Society* 154 (2007): A971, https://doi.org/10.1149/1.2769831.

27. U.-H. Kim, S.-B. Lee, J.-H. Ryu, C. S. Yoon, and Y.-K. Sun, "Optimization of Ni-Rich $Li[Ni_{0.92-x}Co_{0.04}Mn_{0.04}Al_x]O_2$ Cathodes for High Energy Density Lithium-Ion Batteries," *Journal of Power Sources* 564 (2023): 232850, https://doi.org/10.1016/j.jpowsour.2023.232850.

28. H. Chen, T. Aalto, V. Vanita, and O. Clemens, "Effect of Uniaxial Stack Pressure on the Performance of Nanocrystalline Electrolytes and Electrode Composites for All-Solid-State Fluoride-Ion Batteries," *Small Structures* 5 (2024): 2300570, https://doi.org/10.1002/sstr.202300570.

29. J. M. Doux, Y. Yang, D. H. S. Tan, et al., "Pressure Effects on Sulfide Electrolytes for All Solid-State Batteries," *Journal of Materials Chemistry A* 8 (2020): 5049–5055, https://doi.org/10.1039/C9TA12889A.

30. L. Wu, K.-W. Nam, Y. Zhou, et al., "Structural Origin of Overcharge-Induced Thermal Instability of Ni-Containing Layered-Cathodes for High-Energy-Density Lithium Batteries," *Chemistry of Materials* 23 (2011): 3953, https://doi.org/10.1021/cm201452q.

31. S.-M. Bak, E. Hu, Y. Zhou, et al., "Structural Changes and Thermal Stability of Charged $LiNi_xMn_xCo_zO_2$ Cathode Materials Studied by Combined, In Situ, Time-Resolved XRD and Mass Spectroscopy," *ACS Applied Materials & Interfaces* 6 (2014): 22594, https://doi.org/10.1021/am506712c.

32. Y. Ma, J. H. Teo, D. Kitsche, et al., "Cycling Performance and Limitations of $LiNiO_2$ in Solid-State Batteries," *ACS Energy Letters* 6 (2021): 3020–3028, https://doi.org/10.1021/acsenergylett.1c01447.

33. C. Yin, M. Ge, Y. Chung, et al., "High-Nickel Heterostructured Cathodes with Local Stoichiometry Control for High-Voltage Operation," *Small Structures* 4 (2023): 2300236, https://doi.org/10.1002/sstr.202300236.

34. T. Liu, L. Yu, J. Lu, et al., "Rational Design of Mechanically Robust Ni-Rich Cathode Materials via Concentration Gradient Strategy," *Nature Communications* 12 (2021): 6024, https://doi.org/10.1038/s41467-021-26290-z.

35. G. Lee, M. Go, H. Wang, et al., "Localized Defective Zone Formation Driven by Selective Li^+ Extraction Defines the High-Voltage Threshold of $LiNi_{0.6}Co_{0.2}Mn_{0.2}O_2$," *Energy Storage Materials* 85 (2026): 104891, https://doi.org/10.1016/j.ensm.2026.104891.

36. H.-H. Ryu, B. Namkoong, J.-H. Kim, I. Belharouak, C. S. Yoon, and Y.-K. Sun, "Capacity Fading Mechanisms in Ni-Rich Single-Crystal NCM Cathodes," *ACS Energy Letters* 6 (2021): 2726–2734, https://doi.org/10.1021/acsenergylett.1c01089.

37. W. Zhang, D. Schroder, T. Arlt, et al., "(Electro)chemical Expansion during Cycling: Monitoring the Pressure Changes in Operating Solid-State Lithium Batteries," *Journal of Materials Chemistry A* 5 (2017): 9929, https://doi.org/10.1039/C7TA02730C.

38. W. Li, H. Y. Asl, Q. Xie, and A. Manthiram, "Collapse of $LiNi_{1-x-y}Co_xMn_yO_2$ Lattice at Deep Charge Irrespective of Nickel Content in Lithium-Ion Batteries," *Journal of the American Chemical Society* 141 (2019): 5097, https://doi.org/10.1021/jacs.8b13798.

39. R. Koerver, I. Aygun, T. Leichtweiß, et al., "Capacity Fade in Solid-State Batteries: Interphase Formation and Chemomechanical Processes in Nickel-Rich Layered Oxide Cathodes and Lithium Thiophosphate Solid Electrolytes," *Chemistry of Materials* 29 (2017): 5574, https://doi.org/10.1021/acs.chemmater.7b00931.

40. D. Hlushkou, A. E. Reising, N. Kaiser, et al., "The Influence of Void Space on Ion Transport in a Composite Cathode for All-Solid-State-Batteries," *Journal of Power Sources* 396 (2018): 363–370, https://doi.org/10.1016/j.jpowsour.2018.06.041.

41. A. Bielefeld, D. A. Weber, R. Rueß, V. Glavas, and J. Janek, "Influence of Lithium Ion Kinetics, Particle Morphology and Voids on the Electrochemical Performance of Composite Cathodes for All-Solid-State Batteries," *Journal of the Electrochemical Society* 169 (2022): 020539, https://doi.org/10.1149/1945-7111/ac50df.

42. K. Song, X. Pan, S. Li, W. Wu, and C. Yu, "In Situ Grown Multi-Functional Siloxane-Based Organic–Inorganic Hybrid Matrix toward Robust Sulfide-Lithium Metal Interface for All-Solid-State Batteries," *Advanced Functional Materials* 36 (2026): e32071, https://doi.org/10.1002/adfm.202532071.

43. H. Gamo, Y. Maeda, K. Kuratani, et al., "Degradation Processes in Positive Electrode Composites for All-Solid-State Lithium-Ion Batteries Visualized by Scanning Spreading Resistance Microscopy," *Small Methods* 9 (2025): 2500080, https://doi.org/10.1002/smtd.202500080.

44. F. Walther, R. Koerver, T. Fuchs, et al., "Visualization of the Interfacial Decomposition of Composite Cathodes in Argyrodite-Based All-Solid-State Batteries Using Time-of-Flight Secondary-Ion Mass Spectrometry," *Chemistry of Materials* 31 (2019): 3745, https://doi.org/10.1021/acs.chemmater.9b00770.

45. D. H. S. Tan, E. A. Wu, H. Nguyen, et al., "Elucidating Reversible Electrochemical Redox of Li_6PS_5Cl Solid Electrolyte," *ACS Energy Letters* 4 (2019): 2418, https://doi.org/10.1021/acsenergylett.9b01693.

46. J. Auvergniot, A. Cassel, J.-B. Ledeuil, et al., "Interface Stability of Argyrodite Li_6PS_5Cl toward $LiCoO_2$, $LiNi_{1/3}Co_{1/3}Mn_{1/3}O_2$, and $LiMn_2O_4$ in Bulk All-Solid-State Batteries," *Chemistry of Materials* 29 (2017): 3883, https://doi.org/10.1021/acs.chemmater.6b04990.

47. J. Auvergniot, A. Cassel, D. Foix, V. Viallet, V. Seznec, and R. Dedryvère, "Redox Activity of Argyrodite Li_6PS_5Cl Electrolyte in All-Solid-State Li-Ion Battery: An XPS Study," *Solid State Ionics* 300 (2017): 78–85, https://doi.org/10.1016/j.ssi.2016.11.029.

48. Y. Yu, P. Karayaylali, L. Giordano, et al., "Probing Depth-Dependent Transition-Metal Redox of Lithium Nickel, Manganese, and Cobalt Oxides in Li-Ion Batteries," *ACS Applied Materials & Interfaces* 12 (2020): 55865, https://doi.org/10.1021/acsami.0c16285.

49. X. Hu, Z. Zhao, Y. Zhao, et al., "Interfacial Degradation of the NMC/Li_6PS_5Cl Composite Cathode in All-Solid-State Batteries," *Journal of Materials Chemistry A* 12 (2024): 3700–3710, https://doi.org/10.1039/D3TA06092F.

50. J. Park, K. Kim, S. Lee, et al., "Mechano-Electrochemical and Structural Insights into Composition-Driven Behavior of $LiNi_{1-x-y}Co_xMn_yO_2$ ($0.3 < 1\text{-}x\text{-}y \leq 0.8$) Cathodes in Sulfide-Based All-Solid-State Batteries," *Advanced Functional Materials* 36 (2026): e17263, https://doi.org/10.1002/adfm.202517263.

51. E. A. Wu, C. Jo, D. H. S. Tan, et al., "A Facile, Dry-Processed Lithium Borate-Based Cathode Coating for Improved All-Solid-State Battery Performance," *Journal of the Electrochemical Society* 167 (2020): 130516, https://doi.org/10.1149/1945-7111/abb8b3.

52. S. H. Jung, K. Oh, Y. J. Nam, et al., "Li_3BO_3–Li_2CO_3: Rationally Designed Buffering Phase for Sulfide All-Solid-State Li-Ion Batteries," *Chemistry of Materials* 30 (2018): 8190–8200, https://doi.org/10.1021/acs.chemmater.8b03321.

53. H.-W. Chan, J.-G. Duh, and S.-R. Sheen, "Electrochemical Performance of LBO-Coated Spinel Lithium Manganese Oxide as Cathode Material for Li-Ion Battery," *Surface & Coatings Technology* 188 (2004): 116–119, https://doi.org/10.1016/j.surfcoat.2004.08.065.

54. J. Haruyama, K. Sodeyama, and Y. Tateyama, "Cation Mixing Properties toward Co Diffusion at the $LiCoO_2$ Cathode/Sulfide Electrolyte Interface in a Solid-State Battery," *ACS Applied Materials & Interfaces* 9 (2017): 286–292, https://doi.org/10.1021/acsami.6b08435.c.

55. R. Jung, M. Metzger, F. Maglia, et al., "Oxygen Release and Its Effect on the Cycling Stability of $LiNi_xMn_yCo_zO_2$ (NMC) Cathode Materials for Li-Ion Batteries," *Journal of the Electrochemical Society* 164 (2017): A1361, https://doi.org/10.1149/2.0021707jes.

56. S.-K. Jung, H. Kim, S. H. Song, S. Lee, J. Kim, and K. Kang, "Unveiling the Role of Transition-Metal Ions in the Thermal Degradation of Layered Ni-Co-Mn Cathodes for Lithium Rechargeable Batteries," *Advanced Functional Materials* 32 (2022): 2108790, https://doi.org/10.1002/adfm.202108790.

57. H. Banerjee, C. P. Grey, and A. J. Morris, "Stability and Redox Mechanisms of Ni-Rich NMC Cathodes: Insights from First-Principles Many-Body Calculations," *Chemistry of Materials* 36 (2024): 6575–6587, https://doi.org/10.1021/acs.chemmater.4c00928.

58. U.-H. Kim, T.-Y. Yu, J. W. Lee, et al., "Microstructure- and Interface-Modified Ni-Rich Cathode for High-Energy-Density All-Solid-State Lithium Batteries," *ACS Energy Letters* 8 (2023): 809, https://doi.org/10.1021/acsenergylett.2c02715.

59. S. Kobayashi, H. Watanabe, T. Kato, F. Mizuno, and A. Kuwabara, "Atomic-Scale Observations of Oxygen Release Degradation in Sulfide-Based All-Solid-State Batteries with Layered Oxide Cathodes," *ACS Applied Materials & Interfaces* 14 (2022): 39459, https://doi.org/10.1021/acsami.2c06950.

60. Y. Wu, Z. Zhang, D. Wu, et al., "Calendar Aging of Sulfide All-Solid-State Batteries," *Nano Energy* 147 (2026): 111576, https://doi.org/10.1016/j.nanoen.2025.111576.

61. Z. Wang, C. Zhu, J. Liu, S. Qi, and J. Ma, "Electrolyte and Interphase Chemistry for 4.6-V Lithium Metal Batteries Operated below −30 °C," *Energy Materials Advances* 6 (2025): 0138, https://doi.org/10.34133/energymatadv.0138.

62. J. Wesselkaemper, P. Thakre, A. Ward, and A. Z. Haddad, "Primary Material Supply Configurations and Domestic Recycling for Cost-Effective Battery Material Production in the US," *Nature Communications* 17 (2026): 253, https://doi.org/10.1038/s41467-025-66957-5.

63. U.-H. Kim, S.-B. Lee, N.-Y. Park, S. J. Kim, C. S. Yoon, and Y.-K. Sun, "High-Energy-Density Li-Ion Battery Reaching Full Charge in 12 min," *ACS Energy Letters* 7 (2022): 3880, https://doi.org/10.1021/acsenergylett.2c02032.

Supporting Information

Additional supporting information can be found online in the Supporting Information section.